Monthly Notices of the ROYAL ASTRONOMICAL SOCIETY

MNRAS **463,** 2296–2309 (2016) doi:10.1093/mnras/stw2127
Advance Access publication 2016 August 24

Molecular outflows in starburst nuclei

Arpita Roy,[1,2]★ Biman B. Nath,[1] Prateek Sharma[2] and Yuri Shchekinov[3]

[1]*Raman Research Institute, Sadashiva Nagar, Bangalore 560080, India*
[2]*Joint Astronomy Programme and Department of Physics, Indian Institute of Science, Bangalore 560012, India*
[3]*P. N. Lebedev Physical Institute, 53 Leninskiy Prospekt, 119991 Moscow, Russia*

Accepted 2016 August 20. Received 2016 August 20; in original form 2016 May 11

ABSTRACT

Recent observations have detected molecular outflows in a few nearby starburst nuclei. We discuss the physical processes at work in such an environment in order to outline a scenario that can explain the observed parameters of the phenomenon, such as the molecular mass, speed and size of the outflows. We show that outflows triggered by OB associations, with $N_{\rm OB} \geq 10^5$ (corresponding to a star formation rate (SFR)$\geq$1 $M_\odot$ yr^{-1} in the nuclear region), in a stratified disc with mid-plane density $n_0 \sim$ 200–1000 cm^{-3} and scaleheight $z_0 \geq 200(n_0/10^2\,{\rm cm}^{-3})^{-3/5}$ pc, can form molecules in a cool dense and expanding shell. The associated molecular mass is $\geq 10^7\,M_\odot$ at a distance of a few hundred pc, with a speed of several tens of km s^{-1}. We show that an SFR surface density of $10 \leq \Sigma_{\rm SFR} \leq 50\,M_\odot$ yr^{-1} kpc^{-2} favours the production of molecular outflows, consistent with observed values.

Key words: ISM: bubbles – ISM: molecules – intergalactic medium – galaxies: ISM.

1 INTRODUCTION

Observations show that outflows from starburst galaxies contain gas in different phases, which manifest with different emission mechanisms and are probed in different wavelengths. The fully ionized component usually show up through free–free emission and is probed by X-ray observations (Heckman, Armus & George 1990; Strickland et al. 2004). Partially ionized/atomic component are more clumpy than the fully ionized gas, and are probed by line emission from various ions, e.g. Na I, Mg II etc. (Heckman et al. 2000). Outflows from some nearby starburst galaxies have also been observed to contain a molecular component. Understanding the dynamics of this molecular component has become an important issue, in light of recent observations with Atacama Large Millimeter/submillimeter Array (ALMA) and further observations in the future.

Bolatto et al. (2013) observed a molecular outflow in the central region of NGC 253 with a rate of $\geq$3 $M_\odot$ yr^{-1} (likely as large as 9 $M_\odot$ yr^{-1}), with a mass loading factor 1–3. Four expanding shells with radii 60–90 pc have velocities of $\simeq$23–42 km s^{-1}, suggesting a dynamical age of $\sim$1.4–4 Myr. The inferred molecular mass is (0.3–1) $\times$ $10^7\,M_\odot$, and energy $\sim$(2–20) $\times$ 10^{52} erg. These shells likely outline a larger shell around the central starburst region.

Tsai et al. (2012) observed a molecular outflow in NGC 3628 with the CO (J=1–0) line. The outflow shows almost a structureless morphology with a very weak bubble breaking through in the north part of the central outflow. Its size of $\sim$370–450 pc, inferred molecular mass of $\sim 2.8 \times 10^7\,M_\odot$, and outflow speed $\sim 90 \pm 10$ km s^{-1}, suggest a total kinetic energy of molecular gas of $\sim 3 \times 10^{54}$ erg.

More recently, Salak et al. (2016) observed dust lanes above the galactic plane in NGC 1808 along with Na I, N II, CO(1–0) emission lines tracing extraplanar gas close (within 2 kpc) to the Galactic Centre with a mass of $10^8\,M_\odot$, and a nuclear star formation rate (SFR) of $\sim$1 $M_\odot$ yr^{-1}. The velocity along the minor axes varies in the range 48–128 km s^{-1} and most likely indicates a gas outflow off the disc with an estimated mass-loss rate of (1–10) $M_\odot$ yr^{-1}.

The molecular outflow observed in M82 has a complex morphology. The part of it outlined by CO emission is at a larger radii than the part seen with HCN and HCO$^+$ lines. The CO (J=1–0) observations show diffuse molecular gas in a nearly spherical region of radius $\sim$0.75 kpc, with a total molecular mass $3.3 \times 10^8\,M_\odot$, with an average outflow velocity of $\sim$100 km s^{-1} (Walter, Weiss & Scoville 2002). The corresponding kinetic energy of the CO-outflow is of $\sim 3 \times 10^{55}$ erg. More recently, Salak et al. (2014) re-estimated the mass and kinetic energy of CO gas to be larger by factors of 3 and 3–10, respectively. Notably, the molecular outflow morphology is similar to that of the dust halo described by Alton, Davies & Bianchi (1999).

The morphology of the region of the outflow observed in HCN/HCO$^+$ is similar to that of the CO outflow – it is amorphous and nearly spherical with slightly smaller length-scale: the radius of the HCN region is of 400–450 pc, and around 600 pc for HCO$^+$; both HCN and HCO$^+$ emissions show clumpy structure with characteristic size of 100 pc (Salas et al. 2014). The kinematics and the energetics differ slightly from those inferred for the CO-outflow: the mean de-projected outflow velocity for HCO$^+$ is 64 km s^{-1}, while for HCN it is 43 km s^{-1}. The total molecular mass contained into the HCN (HCO$^+$) outflows is $\geq$7(21) $\times$ $10^6\,M_\odot$, which in total is an order of magnitude lower for molecular outflows associated with CO (Walter et al. 2002). The kinetic energy of the outflow associated

★ E-mail: arpita@rri.res.in

with HCN/HCO$^+$ emission ranges between 5 and 30 $\times$ 10^{52} erg. The molecular outflow rate is $\geq$0.3 $M_\odot$ yr^{-1}. They also inferred an SFR of $\sim$4–7 $M_\odot$ yr^{-1} from free–free emission.

These observations pose a number of questions that we address in this paper: are the molecules formed *in situ* in the flow or are they entrained the flow, or are the residues of the parent molecular cloud (in which the superbubble has gone off)? What are the typical length-scales, time-scales, molecular mass and speed? How are these related to the SFR, or disc parameters (e.g. gas density, scaleheight)?

In this paper, we outline a model which includes the basic physical processes for producing a molecular outflow in starburst nuclei, and addresses some of these issues. We have kept our model simple enough to be general, but it has the essential ingredients in order to explain some of the observed parameters mentioned above, namely the length-scales and velocities, as well as an estimate of the molecular mass. Our results can become the base models of more sophisticated numerical simulations which would be able to address finer details of this complex phenomenon.

We use a model of a shell propagating in a stratified interstellar medium (ISM) in our calculation. Such an outflow is inherently two-dimensional, with the dense shell pushed out to a roughly constant stand-off radius in the plane of the disc, while the top of the bubble is blown off by Rayleigh–Taylor instability. In steady state, a dense shell (in which molecules can form) exists in a dynamically young ($r/v \sim$ few Myr) conical shell confined within a few times the scaleheight (see Fig. 2 for a cartoon; for numerical simulations, see figs 2 and 3 of Sarkar et al. 2015). For analytical tractability, we consider the formation and survival of molecules in the dense shell expanding in a stratified disc. All starburst nuclei discussed in the paper show a CO disc and biconical outflows emanating from them. We expect our simple estimates to apply, at least to an order of magnitude, for the realistic scenario.

We begin with a discussion of the phase space of molecular and ionic components of outflows from starbursts, and after eliminating various possibilities we arrive at a basic scenario (Section 2). In the later part of this section, we study various physical constraints on the parameters of the starburst and the disc galaxy for producing molecular outflows. Next, we discuss the physical processes involved in the formation and destruction of molecules in these outflows (Section 3) and present our results in Section 4.

2 ARRIVING AT A PHYSICAL MODEL

2.1 Radius-velocity space of molecular and atomic components

The phase space of the outflows with molecular and ionic components that we introduce below can be instructive in order to arrive at a physical model. Consider the case of a dense shell of a superbubble triggered by an OB association. In the case of a uniform ambient medium density ρ, the position and velocity of the shell are given by

$$r \sim \left(\frac{\mathcal{L}t^3}{\rho}\right)^{1/5}; \quad v \sim \frac{3}{5}\left(\frac{\mathcal{L}}{\rho}\right)^{1/5} t^{-2/5} \approx \frac{3}{5}\left(\frac{\mathcal{L}}{\rho}\right)^{1/3} r^{-2/3}, \quad (1)$$

where $\mathcal{L}$ is the mechanical luminosity driving the superbubble. In other words, the position and velocity of the shell are related as $r \propto v^{-3/2}$. We can first compare this with observational data. However, in order to make a meaningful comparison between galaxies with different SFR, one can take out the dependence on SFR, by plotting $v/(\mathrm{SFR})^{1/5}$ against $r/(\mathrm{SFR})^{1/5}$, since both r and v depend on $\mathcal{L}$ (and consequently, the SFR).

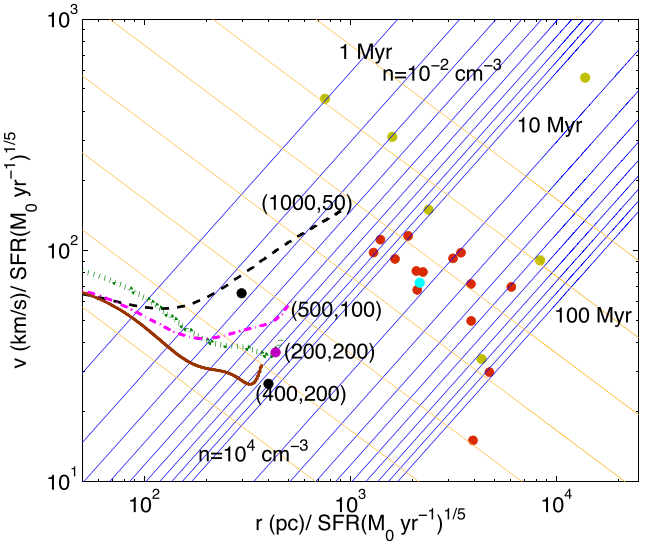

Figure 1. Phase space of molecular and atomic outflows, with points representing different observations of molecular (black and magenta points) and atomic outflows (olive green points), as well as atomic outflows from ULIRGs (red points). The cyan point represent the warm (2000 K) molecular outflow of M82. The black-dashed, green-dotted, magenta-dashed-dotted and the brown solid lines show the simulation results for superbubble evolution with radiative cooling for different combinations of mid-plane density and scaleheight (as labelled, with the first number of the pair being density in cm^{-3} and the second being the scaleheight in pc). Orange solid lines represent the $v-r$ lines for different fixed hydrogen particle densities (of the ambient medium) ranging from 0.01 cm^{-3} (top) to 10^4 cm^{-3} (bottom), and for a given mechanical luminosity injection. The density increases from top to bottom with the increment by a factor of 10 between two consecutive lines. The blue solid lines are for different epochs in the logarithmic scale. The first 10 lines are separated by 1 Myr starting from 1 to 10 Myr, and the rest of the 10 lines have a separation of 10 Myr between two consecutive lines ranging from 10 to 100 Myr.

We show in Fig. 1 data from observations of molecular components from NGC 253 and NGC 3828 (black points), and M82 (HCN component in magenta, and the warm component in cyan). The length-scales and velocities of this component are known from imaging and spectroscopic observations. It is not easy to determine the distances of atomic clouds that are usually probed by absorption lines. However there are a handful of cases of outflows from edge-on galaxies where one has reliable information on the position and speed of the atomic clouds (M82, NGC 3079, 5253, 1482, 4666, 1808). These are shown as olive green points in the same figure. We also show the data of atomic components in outflows from Ultra-Luminous Infrared Galaxies (ULIRG) as red points (from Martin 2005).

We also show as brown slanted lines the simple scaling of $v \propto r^{-2/3}$, for different uniform ambient densities ρ, with the density being the largest in the bottom-left corner ($n_0 = 10^4$ cm^{-3}) and the smallest ($n_0 = 10^{-2}$ cm^{-3}) in the top-right corner of the diagram. The blue lines are the isochrones at different times, starting with 1 Myr from the top and each line separated by 1 Myr from the next, and separated by 10 Myr after the 10 Myr mark.

It is interesting that the molecular and atomic components separate out into different regions in the phase-space. [One cyan point

among the olive green and red points for atomic component refers to the case of warm (2000 K) molecules in M82.] They also separate out with regard to the constant density lines although there are some exceptions. In other words, molecules appear to probe small-scale outflows and high ambient density regions, whereas the atomic components probe large-scale outflows ($\geq$1 kpc) and low ambient density. However, we note that here the length-scales and velocities are normalized by $\mathrm{SFR}^{1/5}$ and so the diagram may not allow such a neat interpretation in terms of length-scales and velocities.

The molecular and atomic components may not appear to be parts of an evolutionary sequence in the context of a uniform ambient medium, but they may be related if the density is not uniform as in the case of a stratified disc gas. We show the evolution of the vertical heights of superbubbles triggered by an association of 10^5 OB stars (the reasons for this choice of parameter will be explained later), in an exponentially stratified medium characterized by mid-plane density n_0 and scaleheight z_0. The dashed, dot–dashed, dotted and solid lines show the cases for different combinations of mid-plane density and scaleheights (labelled by these parameters, n_0 in units of cm^{-3}, and z_0 in pc). The evolutionary tracks are different from slanted lines because of stratification and radiative cooling in the simulations. However, the point to be noted is that the atomic/ionic outflow data points may be connected to the molecular outflow data points through such evolutionary curves of superbubbles in a stratified medium, connecting these two apparently disparate phenomena with an evolutionary sequence.

2.2 Preliminary estimates

These observations lead to a few preliminary estimates. For example, from typical sizes and velocities in observed outflows in NGC 253 and NGC 3068 one infers a dynamical age of $r/v \sim 2$–4 Myr. Assuming that the age of the star cluster associated with the outflow is longer than the main-sequence lifetime of the least massive OB star, i.e. 30 Myr, and with a constant SFR of a few $\mathrm{M}_\odot\ \mathrm{yr}^{-1}$, the total number of supernovae (SNe) exploded during the dynamical time-scale is $\sim 10^5$, and a total SNe energy of $\sim 10^{56}$ erg. The total kinetic energy deposited by these SNe is $\sim 7 \times 10^{55}$ erg. However, when an SN remnant enters the radiative phase, its energy (both kinetic and thermal) is lost and a small fraction remains in the form of kinetic energy. Smith (1993) have shown that the energy of SN remnants decrease as $\propto R^{-2}$ in the radiative phase. Assuming that SN remnants merge with each other earlier than when their radii grow three times since the onset of radiative phase (Nath & Shchekinov 2013), we arrive at the estimate of kinetic energy available for molecular outflow as $\simeq 7 \times 10^{54}$ erg. Therefore, the observed kinetic energy of the molecular outflow ($<10^{53}$ erg s^{-1}) is much smaller than the mechanical energy deposited by stars. This is even smaller than the mechanical energy retained by the superbubble, assuming that 90 per cent of the mechanical energy is lost via radiative cooling (Sharma et al. 2014; Vasiliev, Nath & Shchekinov 2015; Gupta et al. 2016).

These considerations point towards the following scenario. Suppose that the central starburst drives a shell by multiple SNe explosions. A quasi-spherical expanding shock wave from an OB-association becomes unstable against Rayleigh–Taylor and Kelvin–Helmholtz instabilities (the latter begins to be operative when the shock front expands into the halo where the front goes up faster due to decreasing density and a tangential component emerges; Mac-Low, McCray & Norman 1989). In the next stage, the uppermost part of the front breaks and forms an outflow in the vertical direction, while the rest of the shell fragments and forms multiple clouds and clumps moving pervasively within the expanding shell. The expanding molecular gas can be swept up at the observed distance $D \sim 500$ pc by the quasi-spherical shock wave propagating in an exponentially stratified gas layer with the scaleheight $z_0 = 100$ pc and the mid-plane density $n_0 = 3 \times 10^2\ \mathrm{cm}^{-3}$, such that characteristic cooling time at $T \sim 10^6$ K is only 100 yr, and the current observed state of molecular outflow is consistent with the fact the majority of energy has been lost.

We elaborate on this model in the rest of the paper. However, let us consider here briefly the possibility that the molecular clumps are pushed by radiation pressure. Molecular clumps are dense enough to ensure tight collisional coupling between dust and gas particles. In such conditions, the radiation force acting on the clump, and the resulting acceleration, are

$$F_R \sim \frac{\pi R^2}{c}\Phi, \qquad a_R \sim \frac{3}{8}\frac{\Phi}{m_\mathrm{H} N_\mathrm{H} c}, \tag{2}$$

where R is the clump radius, Φ is radiation energy flux, N_H is the column density of the clump, where we explicitly assumed $N_{\mathrm{H}_2} = 2N_\mathrm{H}$. The energy flux can be estimated as $\Phi \sim 300 N_* \mathrm{L}_\odot / 4\pi D^2$, for a Kroupa initial mass function (IMF) with N_* being total number of stars in the underlying central stellar association, D is the distance of clumps from the Galactic Centre. For the same IMF, one can assume $N_* \simeq 100 N_\mathrm{OB}$, N_OB being the number of OB stars in the association. For $D \sim 500$ pc, $N_\mathrm{H} \gtrsim 10^{22}\ \mathrm{cm}^{-3}$ for a typical molecular cloud, one obtains

$$v \sim \sqrt{2\int a_R \mathrm{d}r} \sim 30\ \mathrm{km\ s}^{-1} \times (N_\mathrm{OB}/10^5)^{1/2}\,. \tag{3}$$

Therefore, radiation pressure alone cannot possibly explain the typical length-scale and velocities of the observed outflows. Moreover, although the molecular outflow is dynamically young, the nuclear starburst may be old enough such that most luminous O-stars (producing radiative acceleration) are absent. 1D numerical simulations show that radiative acceleration plays a subdominant role after a few Myr (Gupta et al. 2016).

3 PHYSICAL MODEL

Consider a central OB association embedded in a dense stratified disc. The stratification in the disc is assumed to be exponential, with a scaleheight of z_0 and a mid-plane particle density n_0. The ambient temperature is assumed to be in the range of few tens of K, appropriate for a dense region, with densities in the range of 100–1000 cm^{-3}. The mechanical luminosity arising from stellar processes in the OB association drives a shock through the ambient medium, and this superbubble sweeps up ambient matter, which cools and forms a dense shell. The morphology of the observed molecular outflows (mentioned in Section 1) suggests an epoch when the shell has broken out of the disc, as shown in the schematic diagram in Fig. 2. The observed morphology is shown in grey tones whereas the idealized scenario of a superbubble adopted in this paper is shown with dashed lines. Mac-Low et al. (1989) have shown that most of the mass in the superbubble is confined to regions near the disc. However, for analytical simplicity of a one-dimensional calculation, we assume a quasi-spherical shell, and consider its height as the indicator of its distance. The diagram also shows a zoomed version of the shell, and highlights the region of CO formation which will be our region of interest for the calculation of molecule formation/destruction (Section 4.2). Another schematic zoomed view of the shell is shown on the left that shows the density

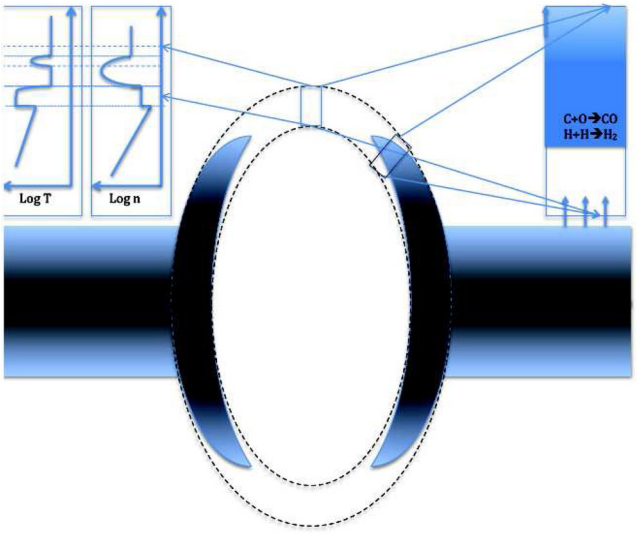

Figure 2. Schematic diagram for the model of outflow used in this paper, with a superbubble shell ploughing through a stratified disc. The observed morphology is shown in grey tones, and the idealized superbubble shell is shown with dashed lines. A zoomed version of the shell is shown on the right, highlighting the region where CO forms (for details, see Section 4.2). The arrows at the bottom of the zoomed shell denote photons incident on the shell. Another zoomed version of the shell is shown on the left that portrays the density and temperature profile in and around the shell. See Section 4.1 for an explanation of this aspect.

and temperature profiles in and around the shell. We will describe this structure in detail in Section 4.1.

The parameters used for the stratified disc (the mid-plane density from 100 to 10^3 cm^{-3}, and the scaleheight 50–200 pc) correspond roughly to a molecular cloud with the surface gas density of $\Sigma_g \simeq (10^3$–$10^4)$M$_\odot$ pc^{-2} [equivalent to typical column densities of molecular clouds N(H) = 10^{23}–10^{24} cm^{-2}], or the total mass of molecular cloud with size $D = 1$ kpc of $M \sim 2 \times 10^8$–10^{10} M$_\odot$ (for $\mu = 2$, where μ is the mean molecular weight).

Consider the minimum size of the OB association needed to explain the observations which show outflowing shell at ∼500 pc with a speed ∼50 km s^{-1}. The observations of a molecular mass of $\geq 10^7$ M$_\odot$ implies a minimum gas density of ∼100 cm^{-3}. For a superbubble expanding in a uniform medium of density ρ, the required mechanical luminosity $\mathcal{L}$ for an outflow to have a speed v at distance r, is given by $\mathcal{L} \approx (5/3)^3 \rho\, v^3 r^2$. The above mentioned observed parameters of speed, distance and density, therefore implies a minimum mechanical luminosity of $\geq 10^{41}$ erg s^{-1}, which corresponds to $\geq 10^5$ OB stars (which we refer to as $N_{\rm OB}$; Roy et al. 2013). We will use this value of $N_{\rm OB}$ as a fiducial number in our work here.

The evolution of the Lyman continuum luminosity of the central source is calculated with STARBURST99 code for instantaneous star formation. We also show the evolution of Lyc and Lyman–Werner band photon luminosities in Fig. 3 for $N_{\rm OB} = 10^5$. Although the mechanical luminosity varies with time, for simplicity we use a constant value (10^{41} erg s^{-1}) as shown by a red dashed horizontal line, and which is a reasonable approximation within the time-scale of 10 Myr considered here. Note the initial rise and subsequent decline in the FUV luminosity (solid line) with time. This behaviour of the FUV luminosity will be important in understanding the evolution of the thermodynamics of the shell, as will be described later in the paper.

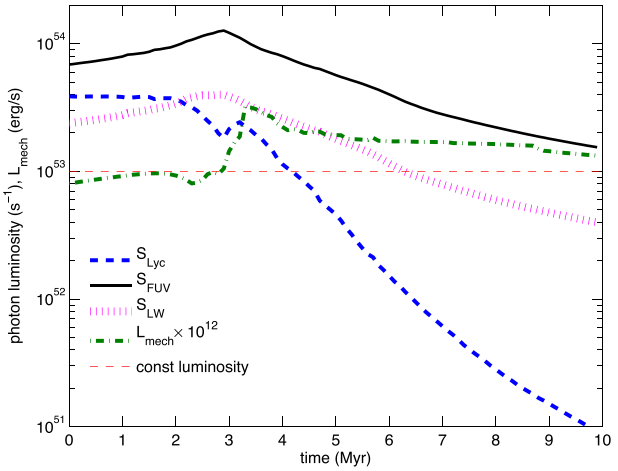

Figure 3. The evolution of mechanical luminosity ($L_{\rm mech}$), Lyman continuum photon luminosity and luminosity in the FUV ($S_{\rm FUV}$), and Lyman–Werner band for $N_{\rm OB} = 10^5$ ($S_{\rm LW}$), calculated using STARBURST99. In this figure, we have plotted $L_{\rm mech} \times 10^{12}$ to accommodate the mechanical luminosity curve along with the other luminosity plots. The slowly growing part on mechanical luminosity on initial stages ($t < 2$ Myr) is due to active stellar wind from massive stars; at $t > 3$ Myr SNe explosions become dominant.

3.1 A flowchart of our calculation strategy

We first describe the formalism of our calculation before discussing the details.

(i) *Dynamics.* We first study the dynamics of a superbubble in a stratified medium. Since the density is large, cooling is important, and therefore the standard solution of Weaver et al. (1977) for uniform media, or the Kompaneets approximation (Kompaneets 1960) for an adiabatic shock wave from a point explosion in a stratified atmosphere, is not adequate. We use hydrodynamical simulations with gas cooling in order to obtain the evolution of the shell. However, in order to focus on the essential physical processes, we only use the vertical height of the shell (denoted here by z_+), and ignore the effects of deviations from sphericity of the shell. We describe the numerical set up in Section A, and use the results of $z_+(t)$ and the corresponding superbubble velocity in our calculation.

(ii) *Thermodynamics*. Given the knowledge of the dynamics of the superbubble, we then discuss the (density and temperature) structure of the shocked gas in Section 4.1. We focus on thermodynamics of the cool, dense shell that forms behind the shock. We assume the density jump between the shell density and the stratified ISM density to be constant in time, for simplicity. Although not precise, this assumption allows us to glean qualitative trends. The estimates of the density jumps are given in Section 4.1 in the presence of the ISM magnetic field. Then, we describe the dominant heating processes (photoelectric – PE – heating) and gas cooling (Section 4.2). The PE heating rate is calculated for the FUV photon luminosity ($S_{\rm FUV}$) with dust extinction (see Appendix D for details). One also needs to have an estimate of the electron density ($n_{\rm e}$) to calculate the PE-heating rate. The diffuse ISM UV photon luminosity is responsible for ionization of the ambient gas, that lies outside the Strömgren sphere for the central source. We calculate $n_{\rm e}$ assuming ionization equilibrium. We solve two coupled equations using thermal equilibrium (equating PE-heating with cooling) and ionization equilibrium to obtain the equilibrium shell temperature [$T_{\rm shell}(t)$], and $n_{\rm e}$. We also demonstrate that the heating and cooling time-scales are much shorter than the dynamical time-scale,

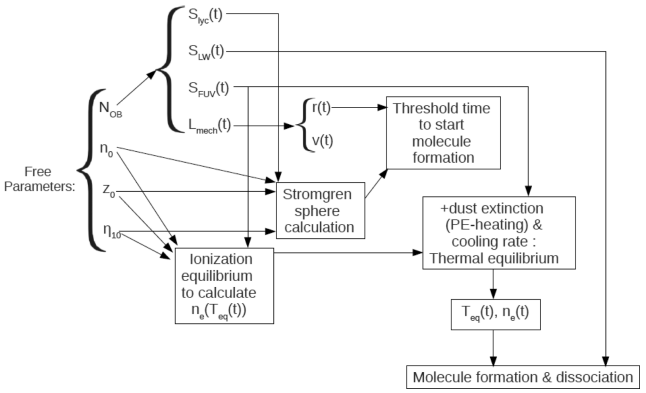

Figure 4. The schematic diagram of the flowchart of the calculation.

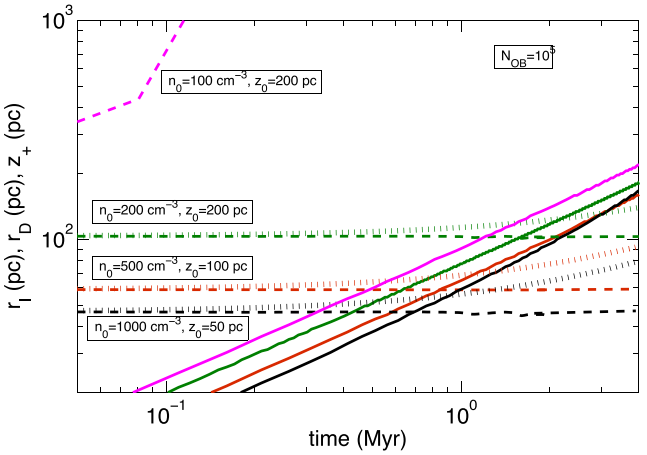

Figure 5. The evolution of the ionization front (the dotted and dashed lines) and the superbubble shell (solid lines), for $N_{OB} = 10^5$ for four sets of n_0–z_0. The black lines represent the maximum density case ($n_0 = 1000$ cm^{-3}, $z_0 = 50$ pc), the red, and the green lines represent $n_0 = 500$ cm^{-3}, $z_0 = 100$ pc, and $n_0 = 200$ cm^{-3}, $z_0 = 200$ pc, respectively. The magenta curve refers to the case of $n_0 = 100$ cm^{-3}, $z_0 = 200$ pc. The dashed lines represent the Strömgren radii for the ambient medium with exponential density stratification, and time varying LyC photon luminosity for the corresponding sets of n_0–z_0. The dotted lines represent the D-type ionization front for the corresponding n_0–z_0 cases.

and thus thermal equilibrium in the shell is a good approximation (Section E).

(iii) *Molecule formation*. Equipped with the knowledge of the density and temperature of the dense shell, we discuss the processes of molecule formation and destruction (using H_2 as a proxy for all molecules) in Section 5, and calculate the amount of molecules formed in the shell in different cases (Section 5.1). The Lyman–Werner band photon luminosity (S_{LW}) is used to calculate the photodissociation of the molecules, after taking into account the effect of dust extinction.

A schematic diagram of the flowchart of the calculation strategy is shown in Fig. 4.

However, the formation of molecules requires some basic conditions to be met. In Section 3.2, we discuss the threshold conditions for molecule formation in the outflowing shell, determined by the ionization due to the OB association.

3.2 Threshold conditions for molecule formation in outflows

When the OB association is born, the initial spurt of ionizing photons will send an ionization front propagating through the surrounding medium, asymptotically forming an ionized zone (Strömgren sphere). The gas will be largely swept-up in a shell such that the remaining gas becomes as dilute as having 2–2.5 orders of magnitude lower density than in the host cloud (Freyer, Hensler & Yorke 2003; García et al. 2013; Dale et al. 2014). At the same time, the SNe and stellar winds arising in the OB association trigger an expanding superbubble that ploughs through the surrounding medium. Conditions inside the ionization front will not support the formation of any molecules, and any existing molecule (entrained from the parent molecular cloud) will likely get photodissociated. Therefore, as long as the superbubble shell is inside the ionization front, its shell will propagate in a low-density environment and will not show any molecules. Initially, the ionization front would always move faster than the superbubble, and molecules cannot form in the shell until it has overtaken the ionization front.

We use hydrodynamical simulation (described in detail in Appendix A) in order to calculate the evolution of the superbubble. The mechanical luminosity driving the superbubble is assumed to be constant in time, $\mathcal{L} \approx 10^{41}$ erg s^{-1} $\times$ ($N_{OB}/10^5$) as obtained from STARBURST99. In order to focus our attention to the basic physical processes, we consider the evolution of the vertical height (z_+) of bubble and compare with the ionization front in that direction.

The evolution of the ionization front r_I is obtained by integrating,

$$\frac{dr_I}{dt} = \frac{(S_{Lyc}(t) - 4\pi r_I^3 \alpha_{H_I} n^2/3)}{4\pi r_I^2 n}, \quad (4)$$

where α_{H_I} is the case B recombination coefficient of hydrogen. We have calculated r_I for the Lyc photon luminosity profile [$S_{Lyc}(t)$] as obtained from STARBURST99, and for an exponentially stratified density structure. As the ionization front propagates, it gives rise to a D-type front, whose distance can be estimated by equation 37.26 of Draine (2011b). The epoch of conversion in to a D-type front can be estimated by equation 37.15 of Draine (2011b).

For simplicity, we have calculated the evolution of the ionization front and the superbubble shell independently. In other words, the shell is assumed to move in a neutral medium, and the ionization front is assumed to move in a uniform density medium. For most cases, except for $n_0 = 100$ cm^{-3}, $z_0 = 200$ pc, the corresponding error is small, because the gas mass within the Strömgren sphere is not large enough to considerably change the dynamics of the shell.

Fig. 5 shows the evolution of the ionization front, and the vertical location of the superbubble shell for four sets of n_0–z_0 values and for $N_{OB} = 10^5$. The figure shows that the Stömgren sphere radius in the different cases is of the order of ∼50–100 pc (shown by the black, red and green dashed lines). The ionization fronts transform to D-type fronts (prior to 0.1 Myr) and expand slowly beyond the Strömgren radii, to reach heights of the order of ∼80–140 pc in ∼4 Myr. At the same time, the corresponding superbubble shells overtake the ionization fronts at heights of the order of ∼60–120 pc.

Fig. 5 also shows that there are two different regimes: at low column densities of the layer $N(H) = n_0 z_0$, the ionization front moves ahead so quickly such that the superbubble shell can never catch up with, and the shell propagates in a low-density ionized gas (as shown by magenta lines). At high column density limit, the shell can overtake the ionization front, as shown by black, red and green solid lines.

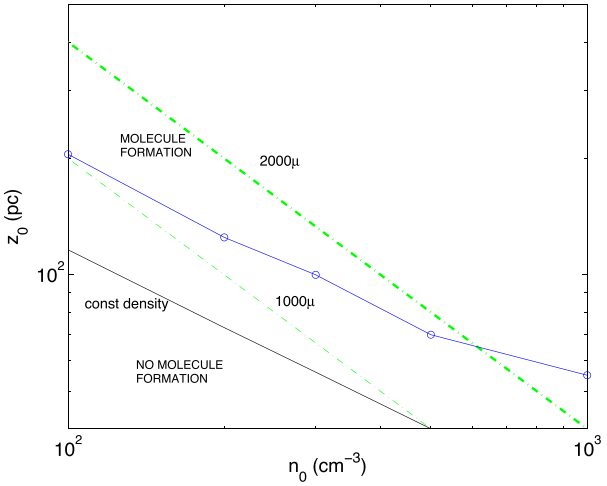

Figure 6. The threshold combination of mid-plane density and scaleheight for the formation of molecules in an outflowing shell triggered by an OB association with $N_{\rm OB} = 10^5$. The blue-solid line represent the cut-off $n_0 - z_0$ condition below which molecules cannot form. The green dash–dotted lines correspond to two values of constant surface densities in units of $\rm M_\odot\ pc^{-2}$, where μ is the mean molecular weight. The black line plots the Strömgren radii for ambient medium with uniform densities for comparison.

It is reasonable to contend that molecular outflows can form behind the SN-driven shock wave only in the latter case. These considerations lead us to determine the locus of the threshold combination of n_0 and z_0 for the formation of molecules in outflowing shell. We show the result with the thin blue solid line in Fig. 6. The curve can be approximated by a fit,

$$z_0 \geq 200\,{\rm pc}\left(\frac{n_0}{10^2\ {\rm cm^{-3}}}\right)^{-3/5}. \quad (5)$$

Note that for a uniform ambient medium of density n_0, and a constant Lyc luminosity of 4×10^{53} photons $\rm s^{-1}$, the Strömgren radius is given by $\sim 116\,{\rm pc}\,(n_0/10^2\ {\rm cm^{-3}})^{-2/3}$. The difference between this estimate and the above fit is due to (a) density stratification and (b) variation of Lyc luminosity with time.

In Fig. 6, we also show lines of constant surface density, marked in the units of $\rm M_\odot\ pc^{-2}$. We find that molecular outflow is possible in a starburst nuclei region with surface density roughly $\geq 1500\,\mu\,({\rm SFR/M_\odot\ yr^{-1}})\,{\rm M_\odot\ pc^{-2}}$.

It is interesting that Nath & Shchekinov (2013) derived a lower limit on the molecular surface density of the order of $1000\ {\rm M_\odot\ pc^{-2}}$ in starburst nuclei for producing outflows. A surface gas density of $\Sigma \sim 1.5 \times 10^3\,\mu\,{\rm M_\odot\ pc^{-2}}$ with $\mu = 1.33$ implies an SFR surface density of $\sim 10\ {\rm M_\odot\ yr^{-1}\ kpc^{-2}}$ from Kennicutt–Schmidt law (Kennicutt 1998). This is incidentally $\sim$100 times larger than the threshold SFR surface density for galactic superwinds (Heckman et al. 2015). Considering a nucleus region of radius $\sim$300 pc, this translates to an SFR of $\geq 3\ {\rm M_\odot\ yr^{-1}}$.

At the same time, our threshold relation also puts an upper limit on the SFR that can produce molecular outflows. Recall that the size of the Strömgren sphere depends on the ratio of $(L_{\rm LyC}/n^2)^{1/3}$. Since the density stratification has rendered a scaling of $z_0 \propto n^{-3/5}$, therefore our threshold condition on the scaleheight likely scales as $N_{\rm OB}^{3/10}$, or $({\rm SFR})^{3/10}$. Recalling that $N_{\rm OB} = 10^5$ corresponds to an SFR of $\sim 0.3\ {\rm M_\odot\ yr^{-1}}$, we can re-write our threshold condition as

$$z_0 \geq 200\,{\rm pc}\left(\frac{n_0}{10^2\ {\rm cm^{-3}}}\right)^{-3/5}\left(\frac{\rm SFR}{0.3\,{\rm M_\odot\ yr^{-1}}}\right)^{3/10}. \quad (6)$$

Considering the size of the central starburst nuclei region to be $\sim$300 pc, we can transform this relation to one involving surface densities. We have

$$\Sigma_{\rm SFR} \leq 50\,{\rm M_\odot\ yr^{-1}\ kpc^{-2}} \times\left(\frac{\Sigma}{1.5\times10^3\,\mu\,{\rm M_\odot\ pc^{-2}}}\right)^{10/3}\left(\frac{n_0}{10^2\ {\rm cm^{-3}}}\right)^{-4/3}. \quad (7)$$

This essentially implies that the SFR has to be lower than a certain value for a given column density of the starburst nucleus; a larger SFR than the above inequality would inhibit the formation of molecules by ionizing the gas in the superbubble shell.

We then have three relevant scales for SFR surface density. A lower limit of $\Sigma_{\rm SFR} \geq 0.1\ {\rm M_\odot\ yr^{-1}\ kpc^{-2}}$ ensures a galactic wind. However, the production of molecular outflows is limited to SFR surface densities $10 \leq \Sigma_{\rm SFR} \leq 50\ {\rm M_\odot\ yr^{-1}\ kpc^{-2}}$. It is interesting to note that the SFR surface densities of galaxies observed to host molecular outflows fall in this range. Therefore, our threshold condition for disc parameters for hosting molecular outflows is consistent with observations. We should, however, emphasize that galaxies show a considerable variation around the Kennicutt–Schmidt law and the above constraint on SFR surface density may not be a strong one.

4 SHELL DENSITY AND TEMPERATURE

Given the knowledge of the threshold density and scaleheight for molecule formation, the next important issues for molecules to form are the heating and cooling in the superbubble shell. In this section, we discuss the heating and cooling processes that play an important role in determining the shell temperature.

4.1 Four-zone structure

From the point of view of the presence of molecular gas in the expanding shell associated with the wind outflow it is convenient to separate the whole post-shock flow on to four distinct zones, which are schematically shown on the left in Fig. 2 (see also fig. 5 of Sharma et al. 2014). The zones described below are shown in the schematic diagram as being separated by dotted lines, from top to bottom: (i) the viscous layer where kinetic energy of the inflowing gas is transformed partly into thermal energy, and the entropy grows to the post-shock value (Zeldovich & Raizer 1966), (ii) the radiative relaxation layer (RRL) where radiative losses lead to the formation of a dense shell, (iii) thin dense shell restricted from the bottom by (iv) the still hot low-density gas formed by the termination shock. Dissipation due to viscous forces brings the gas into a new high-temperature state and vanishes beyond the viscous layer. The thickness of this layer is determined by the viscosity, but for strong shock it can be as thin as a few free-path length of gas particles (Zeldovich & Raizer 1966). In numerical models, its thickness is always unresolved as this thickness is equivalent to a few times the mean-free path. The rate of energy loss due to radiation losses in the second zone depends on post-shock temperature and density and becomes important when the dynamical time becomes comparable to the cooling time.

We show in Appendix C that the density in the cool/dense shell (region iii) can be larger than the ambient density by a factor of a few to $\sim$100. Magnetic field in the ISM prevents the shell density from becoming exceedingly large. We characterize the density in the shell as

$$n_{\rm sh} = 10\,\eta_{10}\,n_{\rm amb}\,, \quad (8)$$

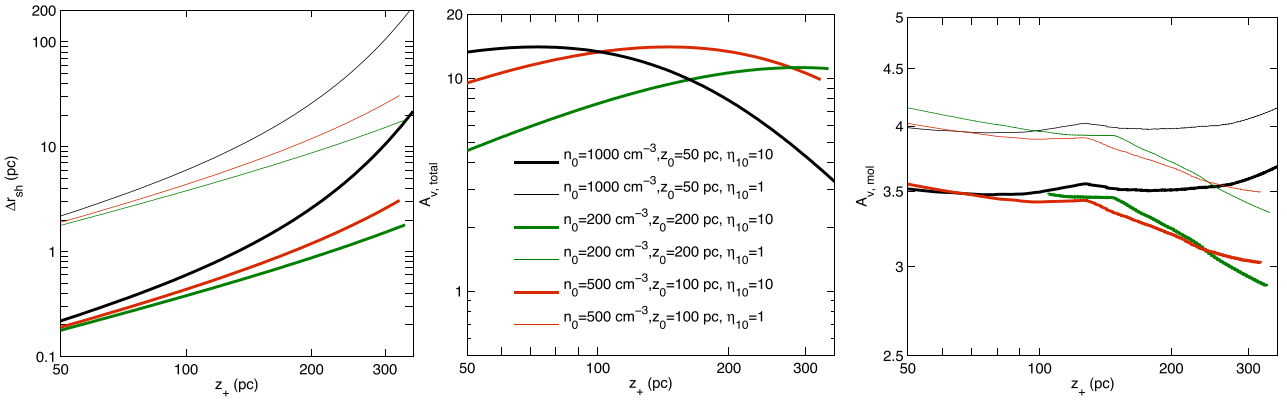

Figure 7. The evolution of the shell thickness and A_v for three mid-plane density and scaleheight combinations for $N_{OB} = 10^5$, and for three different n_0, z_0 cases ($n_0 = 1000$ cm^{-3}, $z_0 = 50$ pc; $n_0 = 200$ cm^{-3}, $z_0 = 200$ pc, and $n_0 = 500$ cm^{-3}, $z_0 = 100$ pc), for two η_{10} cases and for $N_{OB} = 10^5$. The thick and thin solid lines correspond to $\eta_{10} = 10$ and 1, respectively. The black, green, and the red lines represent $n_0 = 1000$ cm^{-3}, $z_0 = 50$ pc; $n_0 = 200$ cm^{-3}, $z_0 = 200$ pc, and $n_0 = 500$ cm^{-3}, $z_0 = 100$ pc cases, respectively. All the plots hereafter follow the same colour and line-styles for the corresponding n_0, z_0, and η_{10} values. The leftmost panel shows the shell thickness as a function of the vertical position of superbubble shell, and the middle panel represents the evolution of total A_v (which does not depend on the value of η_{10}, or in other words, the thin lines coincide with the thick ones). The right-hand panel shows the values of A_v(mol) for the region where molecules form in substantial quantity, and which is the region of our concern.

where $n_{amb} = n_0 e^{-z_+/z_0}$. Given this density jump, the shell thickness ($\triangle r_{sh}$) can be found by equating the total swept up mass to the shell mass,

$$\int_0^{z+} 4\pi z^2 n_0 e^{-z/z_0} dz \approx 4\pi z_+^2 \triangle r_{sh} n_{sh} , \quad (9)$$

which gives the value of $\triangle r_{sh}$. Here, we have assumed the shell to be spherical, which is a reasonable approximation since the spherical shape of superbubble shell is roughly maintained until it reaches a few times (two to three) the scaleheight. The shell thickness is shown in the leftmost panel of Fig. 7 for different cases. The lower set of curves are for $\eta_{10} = 10$ and the upper set of curves, for $\eta_{10} = 1$.

Although the radius and thickness increases with time, since the density in a stratified medium decreases with height, the total column density in the shell does not increase monotonically. It rises until the shell reaches the scaleheight and then decreases. We show the evolution of the total opacity in the shell (proportional to the column density) in the middle panel of Fig. 7. The visual extinction is related to the column density as $A_v \approx (N_H/1.9 \times 10^{21}$ cm$^{-2})$ (Bohlin, Savage & Drake 1978). We find that the maximum visual extinction A_v lies in the range of 10–20, which is attained at roughly the scaleheight. Note that the value of A_v does not depend on the value of density jump.

The temperature in the shell is determined by the balance of heating and cooling processes, which we consider next.

4.2 Heating and cooling processes in the shell

The physical state and ionization structure of the shell resembles the so-called photodissociation region (PDR) considered in the literature (Hollenbach & Tielens 1997). Going outward from the central region, beyond the ionized gas, one first encounters a region of neutral atoms, after which there are regions whose ionization structure is dominated by the influence of FUV photons on different trace elements, beginning with carbon. Here, we focus on the region where CO/H_2 are produced in significant quantity. According to (Wolfire, Hollenbach & McKee 2010, their equation 21), the visual extinction A_v corresponding to CO and H_2 are comparable, and is given by

$$A_v(\text{mol}) \approx 0.1 \ln \left[3.3 \times 10^7 (G_0/1.7n)^2 + 1\right] , \quad (10)$$

where G_0 is the FUV photon density (number of photons per unit volume) obtained from STARBURST99 code.

The rightmost panel of Fig. 7 shows the value of A_v(mol) corresponding to the molecular region that we will focus on, calculated with equation (10). Recall the rise and decline in the FUV luminosity of the central OB association (see Fig. 3). This evolution in the FUV luminosity makes the value of A_v(mol) also rise and then decline (through the term G_0), as seen Fig. 7. For the cases of small scaleheight (solid lines), the shell density decreases rapidly with height, increasing the value of A_v(mol).

The corresponding ionization fraction of the free carbon ions $x_{C^+} \equiv n_{C^+}/n_C$ in the carbon dominated region is given by (Tielens 2005)

$$\frac{1 - x_{C^+}}{x_{C^+}^2} \approx 3.3 \times 10^{-6} \left(\frac{n}{10^4 \text{ cm}^{-3}}\right) \left(\frac{T}{300 \text{ K}}\right)^{-0.6} \times \left(\frac{G_0}{10^4}\right)^{-1} \exp[2.6 A_v] . \quad (11)$$

The ionization fraction therefore is given by $x_e = A_C x_{C^+}$, where $A_C = 1.4 \times 10^{-4}$ is the carbon abundance for solar metallicity. The ionization fraction depends on temperature weakly, and is roughly given by $x_e \approx A_C$, since $x_{C^+} \approx 1$, from equation (11).

The dominant heating process in this region of the shell is PE heating, and it cools through radiation. Given the large density of this region, the temperature is likely to be in the range of ∼10–20 K. We show in Appendix D and E with detailed calculation the values of the ionization fraction and the equilibrium temperature, for different shell densities, and for different cases of n_0 and z_0. The results of the calculation confirms that the ionization fraction $x_e \approx 1.4 \times 10^{-4}$ and that the equilibrium temperature is of the order of ∼10–20 K (which, to be specific, we approximate as 15 K). We assume thermal equilibrium to calculate the shell temperature and x_e, as heating and cooling time-scales of the shell are much shorter than the dynamical time throughout the evolution of the shell. In the following calculations for molecule formation, we adopt these values of x_e and T.

5 MOLECULE FORMATION AND DISSOCIATION

While the observations of molecular outflows have shown that the velocity and the momentum of the molecular component is in rough agreement with the expectations from a star formation driven outflow, the existence of molecules in the outflowing gas is not trivially explained, for the following reasons. The molecular component that is seen at a few hundred pc can either be formed in the outflowing gas, or can be a residue of the molecules entrained from the parent molecular clouds, whatever has survived the destruction process while the shell has evolved and has been shocked. In this section, we study the molecule formation and destruction processes in detail. The two important mechanism for the dissociation of molecules are the photodissociation and the collisional dissociation.

5.1 Formation and destruction of molecules in the shell

Consider the case of a shell propagating outwards, and being irradiated by Lyman–Werner band photons from the OB stars responsible for the outflow in the first place. We consider the formation and dissociation of molecular hydrogen as hydrogen is the most abundant element. Photons in the Lyman–Werner band (11.2−13.6 eV) are responsible for the dissociation of hydrogen molecule. The net rate of formation of molecular hydrogen, for a gas density n, is given by

$$\frac{\mathrm{d}n_{\mathrm{H_2}}}{\mathrm{d}t} = \mathcal{R}_{\mathrm{f}}\, n\, n_{\mathrm{H_I}} - \mathcal{R}_{\mathrm{d,thin}} f_{\mathrm{dust,H_2}}\, f_{\mathrm{shield,H_2}}\, n_{\mathrm{H_2}} - k_D\, n\, n_{\mathrm{H_2}}, \quad (12)$$

where $n_{\mathrm{H_2}}$ is the number density of $\mathrm{H_2}$ molecules. As mentioned above, $\mathcal{R}_{\mathrm{d,thin}}$ depends on the radiation field, and therefore on the distance of the shell from the centre and the luminosity in the Lyman–Werner band. The formation rate $\mathcal{R}_{\mathrm{f}} \approx 3 \times 10^{-18}\, T^{1/2}\ \mathrm{cm^3\ s^{-1}}$ for solar metallicity (Hollenbach & McKee 1979). The density and temperature refers to the shell density and equilibrium temperature calculated in Appendix E.

$\mathcal{R}_{\mathrm{d,thin}} = 3.3 \times 10^{-11}\, G_{\mathrm{LW}}\ \mathrm{s^{-1}}$ is the photodissociation rate in optically thin gas (Draine & Bertoldi 1996), G_{LW} being the strength of the radiation field in units of Habing field. The factor $f_{\mathrm{dust,H_2}}$ takes into account the effects of dust extinction and $f_{\mathrm{shield,H_2}}$, that of $\mathrm{H_2}$ self-shielding. We calculate G_{LW} similar to the equation (D3) with the replacement of S_{FUV} by S_{LW}, albeit without the extinction factor.

For the shielding due to dust, we have

$$f_{\mathrm{dust,H_2}} = \exp(-3.5 A_{\mathrm{v}}(\mathrm{mol}))\,. \quad (13)$$

For the self-shielding due to molecules, we use the fit given by Draine & Bertoldi (1996):

$$f_{\mathrm{shield,H_2}} = \frac{0.965}{(1+x/b_5)^2} + \frac{0.035}{\sqrt{1+x}} \exp\left(-8.5 \times 10^{-4} \sqrt{1+x}\right), \quad (14)$$

where $x = N_{\mathrm{H_2}}/(5 \times 10^{14}\ \mathrm{cm^{-2}})$, $b_5 = b/(10^5\ \mathrm{cm\,s^{-1}})$, $b^2 = kT/m_{\mathrm{H}}$, being the Doppler broadening parameter.

The collisional dissociation is another important dissociation process for destruction of molecules. This process crucially depends on the shell temperature and density. The dissociation rate coefficient $[k_{\mathrm{D}}(n, T)]$ is given by (Lepp & Shull 1983),

$$\log k_{\mathrm{D}}(n, T) = \log k_{\mathrm{H}} - \log(k_{\mathrm{H}}/k_{\mathrm{L}})/(1 + n/n_{\mathrm{cr}})\,, \quad (15)$$

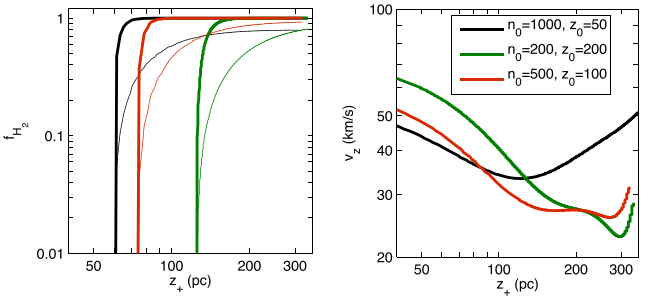

Figure 8. Evolution of molecular fraction (left), and the bubble shell velocity (right) with the size of the superbubble shell, for $N_{\mathrm{OB}} = 10^5$, for different n_0, z_0, and η_{10} cases. The thick and thin lines correspond to $\eta_{10} = 10$ and 1, respectively. All the calculations of molecule formation and dissociation are performed in the dense superbubble shell after it crosses the D-type ionization front.

where $k_{\mathrm{H}}(T)$, and $k_{\mathrm{L}}(T)$ are the dissociation rate coefficients for the high- and low-density limits, respectively, given in table 1 of Lepp & Shull (1983). The critical density n_{cr} depends on temperature and is calculated using equation 6 of Lepp & Shull (1983).

The formation time-scale of molecules is given by

$$t_{\mathrm{form}} \approx (\mathcal{R}_{\mathrm{f}}\, n)^{-1} \approx 10^{-2}\,\mathrm{Myr} \left(\frac{n}{10^3\ \mathrm{cm^{-3}}}\right)^{-1} \left(\frac{T}{100\ \mathrm{K}}\right)^{-1/2}. \quad (16)$$

The photodissociation time-scale of molecules is given by

$$t_{\mathrm{dest}} \approx 7 \times 10^{-7}\,\mathrm{Myr} \left(\frac{S_{\mathrm{LW}}}{10^{53}\ \mathrm{s^{-1}}}\right)^{-1} \left(\frac{r}{100\ \mathrm{pc}}\right)^{2} \times (f_{\mathrm{dust,H_2}}\, f_{\mathrm{shield,H_2}})^{-1}\,. \quad (17)$$

In general, the collisional dissociation time-scale is much longer than the photodissociation time-scale, given the low temperature of the dense shell.

These time-scales should be compared with the dynamical time-scale of the dense shell. We found that the formation time-scale becomes comparable to or shorter than the dynamical time-scales, when the shell size exceeds ∼200 pc, signalling the onset of molecule formation.

5.2 Results

Fig. 8 (left-hand panel) shows the resulting molecular fraction as a function of shell distance for $N_{\mathrm{OB}} = 10^5$, for the fiducial cases. The right-hand panel shows the corresponding velocity of the shell.

There is an abrupt jump in the value of the molecular fraction ($f_{\mathrm{H_2}}$) from a small value of 10^{-6} to a maximum value of 1 for large value of η_{10} (=10) whereas for the case of small η_{10}(=1), $f_{\mathrm{H_2}}$ increases slowly to a maximum value of 0.8−0.9 for all the $\mathrm{n_0}-\mathrm{z_0}$ cases. The sharp rise in the molecular fraction corresponds to the epoch of the shell crossing the ionization front, as discussed in Section 3.2.

The velocity of the superbubble shell for all the $\mathrm{n_0}-\mathrm{z_0}$ cases at ∼100−300 pc is ∼10–40 km s^{-1}, which matches with the velocities of the molecular outflows as seen in observations, particularly of NGC 253 (Bolatto et al. 2013).

Fig. 9 shows the total hydrogen column density and the corresponding molecular column densities, in the left- and right-hand panels, respectively. The total column density plots have been explained earlier in the context of total visual extinction in Fig. 7. The

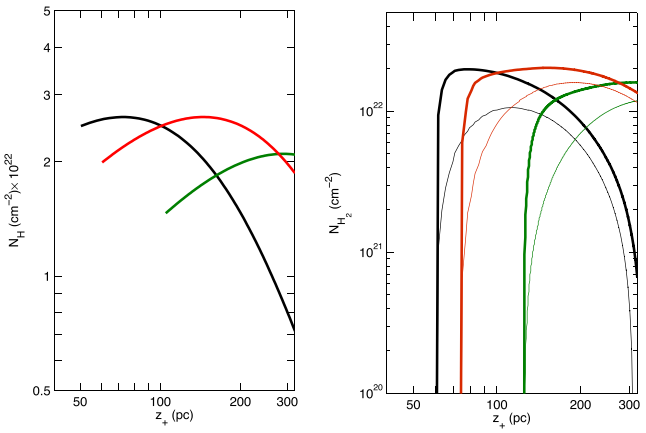

Figure 9. Evolution of the total hydrogen column density (left) and molecular column density (right), with the size of the superbubble shell, for $N_{\rm OB} = 10^5$, for different n_0, z_0, and η_{10} cases. The details of the line-styles and line-colours for different parameters are mentioned in the caption of the Fig. 7.

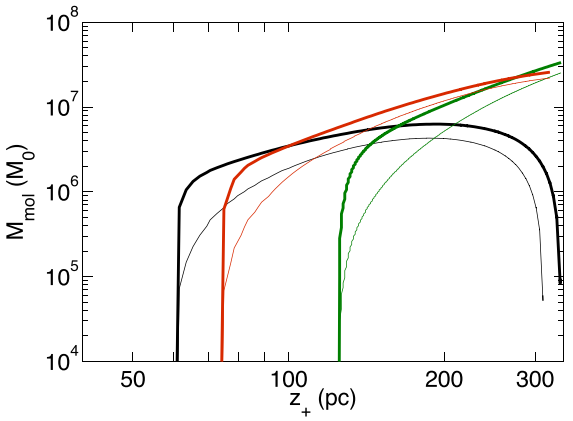

Figure 10. The evolution of molecular mass with the size of the superbubble shell, for $N_{\rm OB} = 10^5$, for three different $n_0 - z_0$ cases, and for the two different values of η_{10} (1, 10). Refer to Fig. 7 for the details of the different line-styles and line-colours. The molecular mass is the integrated mass over the molecular region of the shell.

H_2 column density first rises and then falls due to decreasing shell density and column density. It falls more rapidly in the case of small scaleheight when the gas density rapidly decreases with height.

Fig. 10 shows the evolution of the total molecular mass (integrated over the shell) for different parameters. The molecular mass is found to be in the range of $\sim 10^7$–10^8 $M_\odot$ at $\geq$200 pc, in the three fiducial cases, consistent with observations. As both the dissociation rates (photodissociation and collisional dissociation) are much smaller compared to the formation rate of molecules, for most cases the molecular mass does not decrease as the radius of the superbubble shell increases – rather its rate of increase may slow down, particularly in the case of discs with small scaleheights. For the cases of large mid-plane density and small scaleheight, the molecular mass decreases, as the column density of the shell decreases with increasing height. We note that at larger radii, when the shell crosses a few scaleheights, the shock-heating can be an important mechanism (as the velocity goes up till $\sim 50-100$ km s^{-1}, and also the density of the shell reduces) to destroy the molecules in the dense shell, and thus reducing the molecular mass integrated over the shell. This aspect is beyond the scope of this paper.

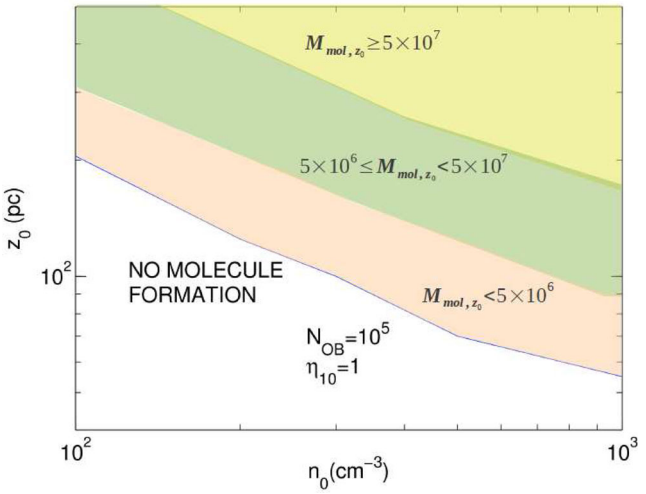

Figure 11. Regions in the parameter space of n_0 and z_0 that can give rise to molecular mass of different ranges in shells triggered by star formation activity, with $N_{\rm OB} = 10^5$, and with $\eta_{10} = 1$. Corresponding CO luminosities are also indicated.

The important parameters that can be used to compare with observations are the molecular mass and the length-scale of the molecular shell (as well as its speed). We wish to determine the ranges in the combination of gas density and scaleheight (for the given $N_{\rm OB} = 10^5$) that can give rise to molecular outflows with a certain molecular mass and radius of the shell. We consider the molecular mass attained at the time of crossing the disc scaleheight. We show in Fig. 11 the regions in the parameter space of n_0 and z_0 that correspond to molecular masses (calculated at the scaleheight) of different ranges. The lower blank portion corresponds to the lower limit of Fig. 6.

6 DISCUSSION

6.1 Previous studies

Despite a rather long history of numerical simulations of galactic winds (see the seminal papers; Suchkov et al. 1994, 1996), only one paper with theoretical analysis of galactic winds published to date appears to be relevant for the formation of molecular outflows. Thompson et al. (2016) described a *steady-state* model of a galactic wind with a detailed description of the thermal processes, such as radiative cooling and thermal conduction, along with a qualitative analysis of thermal instability and convection in the expanding gas. Their study focuses, however, on generic features of such a flow, connecting the central energy and mass source and a distant circumgalactic gas. The inner boundary conditions here are set at $R = 0.3$ kpc from a central energy and mass injection source as described by Chevalier & Clegg (1985), which is actually comparable to the sizes of regions where molecules are already seen in galactic winds. Moreover, gas density ($n \leq 1$ cm^{-3}) and temperature ($T \geq 2 \times 10^3$ K) in the outflow always remain in the range that is unsuitable for the formation of molecules.

A more plausible scenario for the observed molecular outflows, and the one that we favour, is the cooling of the shocked gas in the radiative outer shock. Thompson et al. (2016, see also Sarkar et al. 2016) only consider multiphase cooling in the mass-loaded galactic outflow and not the dense shell. *Steady-state* flows are smooth, showing only a very weak increase in the gas density at $z \gtrsim 10$ kpc

(see fig. 2 of Thompson et al. 2016). In our *non-steady* outflow, the formation of a shock in the very beginning (at scales of a few pc) is an essential event which makes the gas cool down quickly to $T \lesssim 100$ K within a few Myr or less. At this stage, the ambient gas density is quite high and therefore the post-shock density and temperature are in the range $n > 10^3$ cm^{-3} and $T \lesssim$ 10–30 K where molecules can efficiently form. Moreover, these conditions are suitable for line emission of CO and HCN/HCO$^+$.

Girichidis et al. (2016) simulated the effect of SNe driven outflows and studied the effects of clustering and frequency of SNe. Their simulations showed that molecules formed at vertical distances less than the disc scaleheight (their fig. 2). However, their focus was on the velocity dispersion of different phases of gas in a typical disc galaxy, and not on the dynamics and chemistry of expanding shells triggered by large OB associations, as have been observed in starburst nuclei.

We also note that Zubovas & King (2014) considered the formation of molecules in AGN driven outflows. However, their model is more relevant for the formation of molecules in outflows with speed $\sim$1000 km s^{-1} and with mass outflow rates of $\sim$1000 M$_\odot$ yr^{-1}, and is different in scope and nature than the small-scale outflows in starburst nuclei with smaller speeds.

6.2 Comparison with observations

It is readily seen from Fig. 10 that in a wide range of parameter space (n_0, z_0), the model predictions are consistent with the observed molecular outflows. Moreover, numerical models reveal the range of physical parameters under which starbursts generate powerful high-mass molecular outflows. In particular, it is clear from Fig. 10 that for small gas scaleheights z_0 the expanding molecular layers widen, thereby decreasing the column density due to mass conservation $N_{\rm H_2} \propto (z_0/z)^2$ with nearly constant molecular fraction. The decrease in $N_{\rm H_2}$ is faster in models with smaller z_0. As a result, the maximum molecular mass in such models remains relatively low $M_{\rm mol} \sim 10^6$ M$_\odot$, while larger scaleheights can give rise to increasing molecular mass beyond $\sim$300 pc. Unfortunately, observations of molecular winds are yet too few, and such an interrelation between density profiles in gas preceding the starburst cannot be inferred from the available observational data.

In general, our calculations show that competitive processes governing the thermodynamics and chemical kinetics of the shell, *viz*, the heating and ionization by Lyman continuum from the underlying nuclear stellar cluster on one side, and from the shock front on the other, and an additional effect from magnetic pressure – determine the possibility to form and expel high-velocity molecular gas into the outflow. It is seen from Figs 8 and 9 that in general for a given n_0–z_0 pair, the molecular outflow may show distinct paths on the $N_{\rm H_2}-v$ plane, as shown separately in Fig. 12.

We find that the H$_2$ column density grows steeply at a nearly constant velocity when the outflowing shell is small. Then, at higher z the expansion velocity decreases while the H$_2$ column density continues to grow. At a certain point close to the breakout level, the column density starts to decrease and the velocity increases – this path is clearly seen for the case of small scaleheight of $z_0 = 50$ pc (black solid line). For larger values of z_0, the curve $N_{\rm H_2}(v)$ shifts left (decreasing velocity), and the loop occurs at a lower velocity, $v_{\rm min} \propto \rho_0^{-1/3} z_0^{-2/3}$. Even though we show results for a fixed numbers of massive stars $N_{\rm OB}$ in the cluster, this relation allows us to predict that in general the scaling would be $v_{\rm min} \propto N_{\rm OB}^{1/3} \rho_0^{-1/3} z_0^{-2/3}$, as follows from a simple wind model in an exponential density profile.

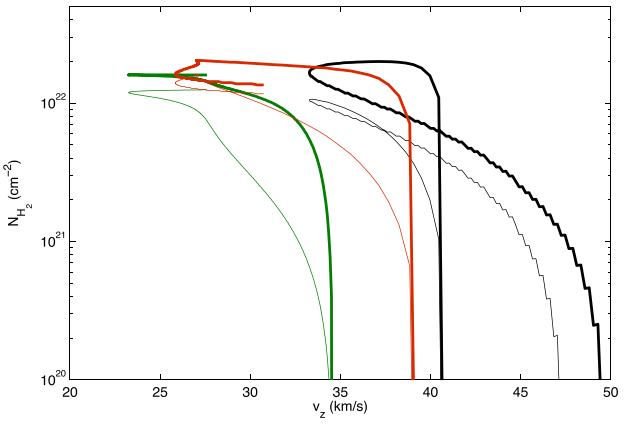

Figure 12. Molecular column density is plotted against the expansion velocity. The line-styles correspond to the same cases as in Fig. 7.

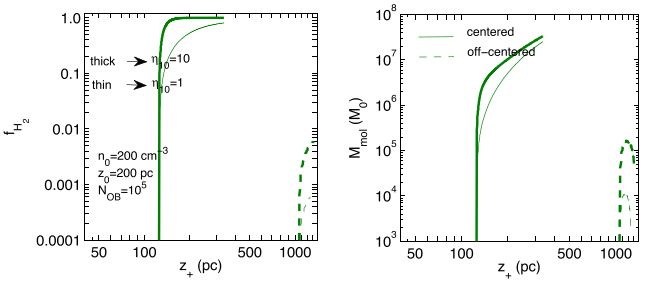

Figure 13. Molecular fraction and molecular mass for an off-centred superbubble (centred at $z' = z_0$) are compared with the case of superbubbles located at the mid-plane, for $n_0 = 200$ cm^{-3} and $z_0 = 200$ pc.

It is worth noting that in realistic conditions the molecular layer is expected to disintegrate due to Rayleigh–Taylor instability with fragments moving outwards nearly ballistically, with the velocity close to the minimum velocity at the loop. In general, the velocity range spanned by the paths agrees with observations. One can therefore expect that the range of observed velocities in molecular outflows relates to the central gas density, its scaleheight and likely the number of massive stars, and may help to constrain them.

6.3 Off-centred shells

We have considered the OB associations that trigger the expanding shells to be located at the mid-plane for simplicity of calculations. However, in reality it could be situated at some height $z' \le z_0$, the scaleheight. Below, we briefly consider the case of off-centred expanding shells. As an extreme case, we show in Fig. 13 the case of a superbubble triggered by an association at a height $z' = z_0$, and compare the molecular fraction and molecular mass with those of a superbubble located at mid-plane.

In the case of an off-centre location of stellar cluster, there are two competing factors: (1) the decreasing column density of the shell and (2) the large distance traversed by the ionization front, because of density stratification. The column density of the shell roughly decreases as (since the accumulated mass is being distributed over the expanding shell)

$$N_{\rm H} \approx \frac{n_0 z_0}{3} \left(\frac{z_0}{z_+ - z'} \right)^2 . \qquad (18)$$

When the shell crosses the ionization front at $z_{\rm I}$, the visual extinction should exceed a critical value ($\sim$3) in order to form a substantial amount of molecules. In other words,

$$\frac{n_0 z_0}{3 \times 1.9 \times 10^{21}\,{\rm cm}^{-2}} \left(\frac{z_0}{z_{\rm I} - z'}\right)^2 \geq 3\,. \quad (19)$$

In this case illustrated above, for $n_0 = 200$ cm^{-3}, $z_0 = 200$ pc, and $z' = z_0$, the ionization front quickly reaches $z_{\rm I} \sim 1$ kpc. Therefore, the above condition is not satisfied and molecules do not form in substantial quantity. This estimate could, in principle, put constraints on the height z'/z_0 of the stellar cluster that can trigger a molecular outflow. However, one could argue that such a large OB association (with $N_{\rm OB} = 10^5$) is likely to be located close to the mid-plane, where the density is highest, rather than being far above the disc. Another point to note is that the expansion speed of an off-centred expanding shell will increase monotonically, if $z/z_0 \sim 1$, and will not have any loops as shown in Fig. 12.

6.4 Caveats

We had set out to understand the dynamical parameters of observed molecular outflows in nearby starburst galaxies, namely, the length-scales and velocities, as well as the corresponding molecular masses. We also sought to understand the possible range of parameters for producing molecular outflows in highly energetic winds. Our 1D calculations, with simplified assumptions of molecule formation in a spherical shell, show that it is possible to understand the observed outflow sizes ($\geq$50 pc) and velocities ($\sim$30–100 km s^{-1}) in the context of superbubbles triggered by starburst activity. The corresponding predicted molecular masses are of order several times 10^6–10^7 M$_\odot$, also consistent with observations of NGC 253 and NGC 3628. The morphology, dynamics and molecular masses of M82 are admittedly not explained by our simplified model, and therefore we wish to point out various caveats in our calculations.

To begin with, it is not possible to discuss the morphologies of observed molecular outflows with a 1D calculation, and as a first step towards understanding this phenomenon our strategy has been to assume a spherical shell. In reality, this shell is likely to fragment, especially after the shell has broken out of the disc, due to thermal and Rayleigh–Taylor instabilities (Roy et al. 2013). Therefore, the covering factor of the shell is likely to be much smaller than unity, allowing radiation and gas to leak through. This is consistent with the observation of Hα radiation from gas far beyond the molecular outflow in M82, for example. These considerations imply that our estimate of molecular mass is at best approximate, and should be viewed/used with caution. As we mentioned in the introduction that the morphology and dynamics of molecular outflows are diverse, and therefore a better estimate would have to consider the details of the PDR region in the shell, and possible clumping in it, as well as the differences in the formation/destruction processes for different molecules, which are beyond the scope of this paper.

7 SUMMARY AND CONCLUSIONS

We summarize our main findings as follows.

(i) We have considered a simple 1D model of molecule formation in expanding superbubble shells triggered by star formation activity in the nuclei of starburst galaxies. We have determined a threshold condition (equation 5) for disc parameters (gas density and scaleheight) for the formation of molecules in superbubble shells breaking out of disc galaxies. This threshold condition implies a gas surface density of $\geq$2000 M$_\odot$ pc^{-2}, which translates to an SFR of $\geq$3 M$_\odot$ yr^{-1} within the nucleus region of radius $\sim$300 pc, consistent with observed SFR of galaxies hosting molecular outflows. We also show that there is a range in the surface density of SFR that is most conducive for the formation of molecular outflows, given by $10 \leq \Sigma_{\rm SFR} \leq 50$ M$_\odot$ yr^{-1} kpc^{-2}, consistent with observations.

(ii) Consideration of molecule formation in these expanding superbubble shells predicts molecular outflows with velocities $\sim$30–40 km s^{-1} at distances $\sim$100–200 pc with a molecular mass $\sim 10^6$–10^7 M$_\odot$, which tally with the recent ALMA observations of NGC 253.

(iii) We have considered different combinations of disc parameters and the predicted velocities of molecule bearing shells in the range of $\sim$30–100 km s^{-1} with length-scales of $\geq$100 pc are in rough agreement with the observations of molecules in NGC 3628 and M82.

ACKNOWLEDGEMENTS

We would like to thank Eve Ostriker for valuable discussions and an anonymous referee for useful comments. The paper is supported partly (YS) by RFBR (project codes 15-02-08293 and 15-52-45114-IND). YS is also thankful to the Grant of the President of the Russian Federation for Support of the Leading Scientific Schools NSh-4235.2014.2.

REFERENCES

Alton P. B., Davies J. I., Bianchi S., 1999, A&A, 343, 51
Bohlin R. C., Savage B. D., Drake J. F., 1978, ApJ, 224, 132
Bolatto A. D. et al., 2013, Nature, 499, 450
Chevalier R. A., Clegg A. W., 1985, Nature, 317, 44
Dale J. E., Ngoumou J., Ercolano B., Bonnel I. A., 2014, MNRAS, 442, 694
Draine B. T., 2011a, ApJ, 732, 100
Draine B. T., 2011b, Physics of the Interstellar and Intergalactic Medium. Princeton Univ. Press, Princeton, NJ
Draine B. T., Bertoldi F., 1996, ApJ, 468, 269
Freyer T., Hensler G., Yorker H. W., 2003, ApJ, 594, 888
García J., Elhoussieny E. E., Bautista M. A., Kallman T. R., 2013, ApJ, 775, 8
Girichidis P. et al., 2016, MNRAS, 456, 3432
Gupta S., Nath B. B., Sharma P., Shchekinov Y., 2016, MNRAS, preprint (arXiv:1606.09127)
Hayes J. C., Norman M. L., Eiedler R. A., Bordner J. O., Li P. S., Clark S. E., ud-Doula A., Mac Low M-M, 2006, ApJS, 165, 188
Heckman T. M., Armus L., George K. M., 1990, ApJS, 74, 833
Heckman T. M., Lehnert M. D., Strickland D. K., Armus L., 2000, ApJ, 129, 493
Heckman T. M., Alexandroff R. M., Borthakur S., Overzier R., Leitherer C., 2015, ApJ, 809, 147
Hollenbach D., McKee C. F., 1979, ApJS, 41, 555
Hollenbach D., Tielens A. G. G. M., 1997, ARA&A, 35, 197
Kennicutt R. C., Jr, 1998, ApJ, 498, 541
Kompaneets A. S., 1960, Sov. Phys. Dokl., 5, 46
Lepp S., Shull J. M., 1983, ApJ, 270, 578
Mac-Low M. M., McCray R., Norman M. L., 1989, ApJ, 337, 141
Martin C., 2005, ApJ, 621, 227
Nath B. B., Shchekinov Y., 2013, ApJ, 777, L12
Roy A., Nath B. B., Sharma P., Shchekinov Y., 2013, MNRAS, 434, 3572
Salak D., Nakai N., Miyamoto Y., Yamauchi A., Tsuru T. G., 2013, PASJ, 65, 66
Salak D., Nakai N., Hatakeyama T., Miyamoto Y., 2016, ApJ, 823, 68
Salas P., Galaz G., Salter D. Herrera-Camus R., Bollatto A. D., Kepley A., 2014, ApJ, 797, 134

Sarkar K. C., Nath B. B., Sharma P., Shchekinov Y., 2015, MNRAS, 448, 328
Sarkar K. C., Nath B. B., Sharma P., Shchekinov Y., 2016, ApJ, 818, L1
Sharma P., Roy A., Nath B. B., Shchekinov Y., 2014, MNRAS, 443, 3463
Smith M. D., 1993, A&A, 272, 571
Strickland D. K, Heckman T. M., Colbert E. J. M., Hoopes C. G., Weaver K. A., 2004, ApJ, 606, 829
Suchkov A. A., Balsara D. S., Heckman T. M., Leitherer C., 1994, ApJ, 430, 511
Suchkov A. A., Berman V. G., Heckman T. M., Balsara D. S., 1996, ApJ, 463, 518
Sutherland R. S., Dopita M. A., 1993, ApJS, 88, 253
Thompson T. A., Quataert E., Zhang D., Weinberg D. H., 2016, MNRAS, 455, 1830
Tielens A. G. G. M., 2005, The Physics and Chemistry of Interstellar Medium. Cambridge Univ. Press, Cambridge
Tsai A.-L., Matsushita S., Kong K. H., Matsumoto H., Kohno K., 2012, ApJ, 752, 38
Vasiliev E. O., Nath B. B., Shchekinov Y., 2015, MNRAS, 446, 1703
Walter F., Weiss A., Scoville N., 2002, ApJ, 580, L21
Weaver R., McCray R., Castor J., Shapiro P., Moore R., 1977, ApJ, 218, 377
Wolfire M. G., McKee C. F., Hollenbach D., 2003, ApJ, 587, 278
Wolfire M. G., Hollenbach D., McKee C. F., 2010, ApJ, 716, 1191
Zeldovich Ya. B., Raizer Yu. P., 1966, Physics of Shock Waves and High-Temperature Hydrodynamic Phenomena. Academic Press, New York
Zubovas K., King A. R., 2014, MNRAS, 439, 400

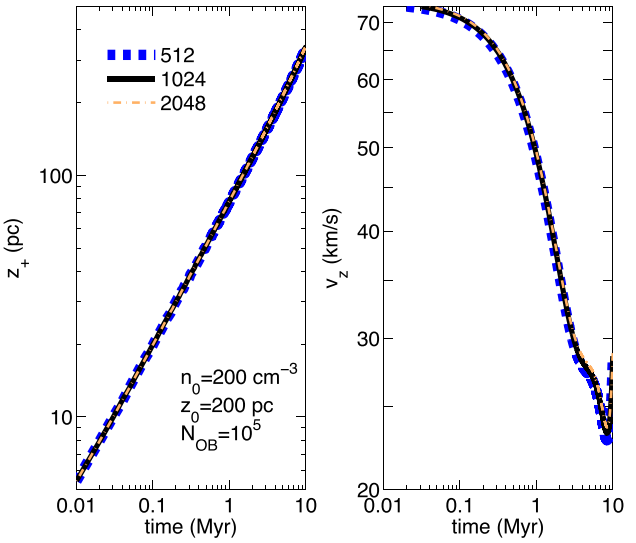

Figure A1. The time evolution of superbubble shell position and velocity for $n_0 = 200$ cm^{-3}, $z_0 = 200$ pc, and for $N_{\rm OB} = 10^5$. The left-hand panel shows the shell position, and the right-hand panel represents the shell velocity. The blue-dashed, the black-solid, and the light brown dash–dotted lines are for 512, 1024 and 2048 grid points, respectively.

APPENDIX A: NUMERICAL SETUP

In this section, we describe our simulation set up. We use a second-order Eulerian, hydrodynamic code (ZEUS-MP code; Hayes et al. 2006). We perform a 1D simulation to get superbubble radius, and velocity. The equations governing superbubble evolution (see also Roy et al. 2013) are given by

$$\frac{{\rm d}\rho}{{\rm d}t} = -\rho\nabla\cdot\boldsymbol{v} + S_\rho(r)\,, \tag{A1}$$

$$\rho\frac{{\rm d}\boldsymbol{v}}{{\rm d}t} = -\nabla p\,, \tag{A2}$$

$$\frac{{\rm d}e}{{\rm d}t} = -q^-(n,T) + S_{\rm e}(r)\,, \tag{A3}$$

where ρ, $\boldsymbol{v}$, and e (=$3p/2$) are the fluid density, velocity, and internal energy, respectively, p is the thermal pressure of the medium; S_ρ, $S_{\rm e}$ are the mass and energy source terms, respectively, $q^- = n_{\rm e}n_i\Lambda(T)$ is the energy loss term due to radiative cooling where $n_{\rm e}$ (n_i), $\Lambda(T)$ are the electron (ion) number density, and the cooling function, respectively. We used Sutherland & Dopita (1993) cooling function for a temperature ranging from 10^4 to 10^9 K for solar metallicity; below 10^4 K we used $\Lambda(T)$ for molecular cooling for an electron fraction ($x_{\rm e} = n_{\rm e}/n_{\rm H}$) of $\sim10^{-3}$, guided by the observed the ionization fraction for cold neutral medium, $\sim10^{-3}$–10^{-4}(Draine 2011b). The cooling function is also independent of $x_{\rm e}$, for $10^{-4} < x_{\rm e} < 10^{-2}$, between 10 and 10^4 K. We have assumed the initial isothermal ambient medium temperature to be 10 K.

The initial ambient density is exponentially stratified and is given by $n = n_0\exp(-|r|/z_0)$, where n_0 and z_0 are the mid-plane density and the scaleheight, respectively. We implement the SNe explosion energy within a small radius ($r_{\rm in}$) so that a strong shock can move through the ISM even after the radiative losses (Sharma et al. 2014). The energy source function [$S_{\rm e} = \mathcal{L}/(4\pi r_{\rm in}^3)$] represents the energy input in SNe within radius $r_{\rm in}$, where $\mathcal{L}$ is mechanical luminosity by SNe. We implement continuous mechanical luminosity till the lifetime of OB association (10 Myr), $\mathcal{L} = 10^{37}N_{\rm OB}$ erg s^{-1} (mechanical luminosities from stellar winds and SN explosions) as obtained from STARBURST99. The mass source function mimics the mass injection in SNe. Therefore $S_\rho = \dot{M}_{\rm in}/(4\pi r_{\rm in}^3)$, where $M_{\rm in}$ is the mass ejected by $N_{\rm OB}$. We choose the ejected mass in each SN explosion to be ~1 M$_\odot$ as superbubble evolution is independent of the mass injection rate. We assume the injection radius $r_{\rm in}$ to be 2 pc in all our simulations. We also assume the CFL number to be 0.2 as it is found to be more robust.

We have used spherical (r, θ, ϕ) coordinate in all our simulations. We start our simulation grid from $r_{\rm min} = 1$ pc ($<r_{\rm in}$), and the outer boundary extends to $r_{\rm max}$ (2.5 kpc). To obtain a better resolution in smaller scales, we use logarithmically spaced grid points along radial direction. The number of grid points between $r_{\rm min}$ and $(r_{\rm min}r_{\rm max})^{1/2}$ are the same as the number of grids between $(r_{\rm min}r_{\rm max})^{1/2}$ and $r_{\rm max}$. The $\theta-$boundary runs from 0 to π, and the $\phi-$boundary extends from 0 to 2π. We adopt the inflow–outflow boundary condition at the inner boundary, and the outflow boundary condition at the outer boundary in the radial direction.

In the r-direction, we use 512 grid points to calculate the evolution of superbubble shell. We show that the time evolution of superbubble shell position is similar for different resolutions with a maximum percentage change of 10 per cent (see Appendix B). We also show that the velocity evolution for different resolutions are also similar (read Appendix B). We adopt $n_0 = 200$ cm^{-3} and $z_0 = 200$ pc to be the fiducial case.

APPENDIX B: CONVERGENCE TEST

We show the time evolution of the shell position and velocity for three resolutions (512, 1024 and 2048 grid points), and for $n_0 = 200$ cm^{-3}, $z_0 = 200$ pc and $N_{\rm OB} = 10^5$. The left-hand panel shows the time evolution of the shell position, and the right-hand panel represents the shell velocity.

One can notice that superbubble shell positions for the three resolution are comparable. The low-resolution runs (512, 1024 grid points) show a similar evolution, whereas the high-resolution case (2048 grid points) varies slightly from the low-resolution cases with

a maximum percentage change being of the order of ∼10 per cent. One can also notice that the velocity evolutions show similar results as in the case of the evolution of the shell positions (showing that the low-resolution runs are similar, and a maximum percentage change of 10 per cent for the case of 2048 grid points). Therefore, we run all our numerical simulation with 512 grid points with an error of ∼10 per cent in both the cases of the shell position, and velocity evolution.

APPENDIX C: DENSITY JUMP IN THE SUPERBUBBLE SHELL

Since the formation of molecules takes place in the cool/dense shell (region iii), it is important to estimate its density. Let (ρ_1, u_1) and ρ_3, u_3 be the density and velocity of the ISM (region i) and the shell (region iii), respectively, in the shock rest frame. The conservation of mass, momentum, and magnetic flux gives

$$\rho_1 u_1 = \rho_3 u_3; \tag{C1}$$

$$\rho_1 u_1^2 + p_1 + p_{\rm mag,1} = \rho_3 u_3^2 + p_3 + p_{\rm mag,3}; \tag{C2}$$

$$B_1 u_1 = B_3 u_3; \tag{C3}$$

where $p_{1,3}$ ($p_{\rm mag1,3} \equiv B_{1,3}^2/[8\pi]$) is the gas (magnetic) pressure in region (i), (iii), and $B_{1,3}$ is the field strength in region (i) and (iii). We assume the field lines to be in the shock-plane (this component is important in preventing the shell to be compressed to very high densities). All the cooling is concentrated in region (ii), and the temperatures T_1 and T_3 correspond to the stable thermal equilibrium temperatures in regions (i) and (iii) (this replaces the energy equation, required to solve for downstream quantities in region iii; see fig. 5 in Sharma et al. 2014). Lets define the compression ratio $r = \rho_3/\rho_1 = u_1/u_3 = B_3/B_1$. Then, equations (C1)–(C3) and the temperature information gives

$$\frac{r^3}{\beta_1} + \left(\frac{c_3}{c_1}\right)^2 r^2 - \left(1 + \mathcal{M}_1^2 + \frac{1}{\beta_1}\right) r + \mathcal{M}_1^2 = 0, \tag{C4}$$

where $c_{1,3}^2 \equiv \gamma_{1,3} k_B T_{1,3}/(\mu_{1,3} m_{\rm p})$ is the sound speed, $\mathcal{M}_1 \equiv u_1/c_1$ is the upstream Mach number, and $\beta_1 \equiv 8\pi p_1/B_1^2$ is the upstream plasma β. Equation (C4) can be solved numerically for various parameters $(\beta_1, \mathcal{M}_1, c_3/c_1)$.

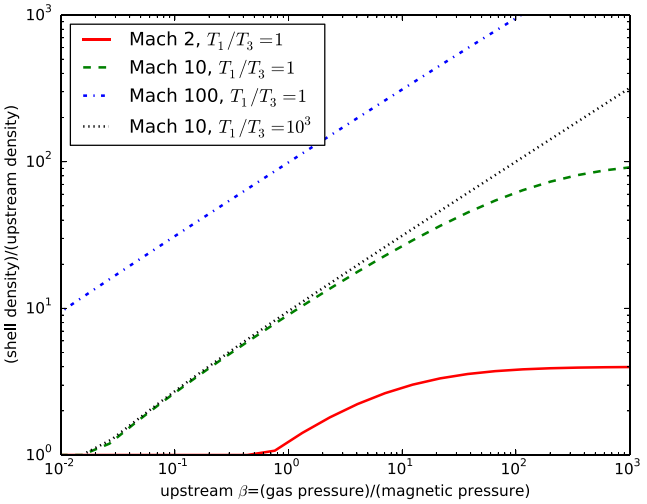

Figure C1. Compression factor (numerical solution of equation C4) as a function of upstream β_1 for various values of the upstream Mach number. The influence of the ratio of the temperatures in regions (i) and (iii) is small in the relevant β_1 regime.

Fig. C1 shows the compression factor as a function of a reasonable range in upstream plasma β for three different Mach numbers, assuming the same temperature in regions (i) and (iii) ($c_1 = c_3$). As expected, the compression factor is larger for a higher Mach number. The compression factors with a reasonable upstream magnetic field $\beta \sim 1$ is much smaller than the hydrodynamic limit ($r \sim \mathcal{M}_1^2$ as $\beta \rightarrow \infty$). A reasonable value for ρ_3/ρ_1 for typical ISM β is in the range few to 100 (see also Smith 1993).

APPENDIX D: HEATING AND COOLING IN THE SHELL

The dominant heating process in the molecular region of the shell is PE heating. We use the PE heating rate given by Wolfire, McKee & Hollenbach (2003), in which they take into account the electron–PAH collisions by the term $\phi_{\rm PAH}$ (which takes into account the fraction of PAH). At a given density, the heating rate depends on the electron abundance, the diffuse incident UV radiation, temperature of the medium, and $\phi_{\rm PAH}$. Therefore, the heating rate per unit volume is given by

$$n\Gamma_{\rm pe} = 1.3 \times 10^{-24} n \epsilon G_{\rm FUV}\ {\rm erg\ cm^{-3}\ s^{-1}}, \tag{D1}$$

where n is the density of the hydrogen nucleus, $G_{\rm FUV}$ is the incident UV radiation field with the dust-extinction (see equation D3) in terms of the Habing radiation, and ϵ is the heating efficiency given by

$$\epsilon = \frac{4.9 \times 10^{-2}}{1 + 4.0 \times 10^{-3} (G_{\rm FUV} T^{1/2}/n_{\rm e}\phi_{\rm PAH})^{0.73}} + \frac{3.7 \times 10^{-2} (T/10^4)^{0.7}}{1 + 2.0 \times 10^{-4} (G_{\rm FUV} T^{1/2}/n_{\rm e}\phi_{\rm PAH})}, \tag{D2}$$

(Draine 2011a), where T is temperature of the medium, $n_{\rm e}$ is the electron density. The heating rate weakly depends on $\phi_{\rm PAH}$ value varying from 0.25 to 1 (Wolfire et al. 2003). In our calculation, we have assumed the value of $\phi_{\rm PAH} \sim 0.5$.

We assume a central OB association at the centre of the galactic disc. We use the STARBURST99 code to calculate the FUV (5.4−13.6 eV) photon luminosity ($S_{\rm FUV}$) (see Fig. 3 in Section 3) to obtain $G_{\rm FUV}$ as a function of z_+ as

$$G_{\rm FUV}(z_+) = \frac{(S_{\rm FUV} \exp(-\tau_{\rm FUV})/4\pi z_+^2)}{(4 \times 10^{-14} c/h\nu_{1000\text{Å}})} = \frac{(S_{\rm FUV} \exp(-\tau_{\rm FUV})/4\pi z_+^2)}{6 \times 10^7}, \tag{D3}$$

where c is the speed of light, $\tau_{\rm FUV}[= \sigma_{\rm d} A_{\rm v}({\rm mol}) \times 1.87 \times 10^{21}]$ is the optical depth of the shell for the FUV photons for the dust extinction cross-section of $\sigma_{\rm d}$. We have considered $\sigma_{\rm d}$ at 1000 Å to be $\sim 6 \times 10^{-22}$ cm^2 for dense clouds with reddening parameter of $R_{\rm v} = 5.5$ (Draine & Bertoldi 1996). We have used the fact that Habing field has an energy density of 4×10^{-14} erg cm^{-3} at 1000 Å (Draine & Bertoldi 1996).

We show the PE heating in Fig. D1 for the two fiducial cases. We calculate the PE-heating rate once the shell crosses the Strömgren sphere radius for all the three combinations of n_0, z_0. We notice that PE-heating depends on electron density, and FUV luminosity, and the equilibrium shell temperature. On the other hand, the electron density depends on the shell density and temperature (as recombination is temperature dependant) which in turn is determined by the

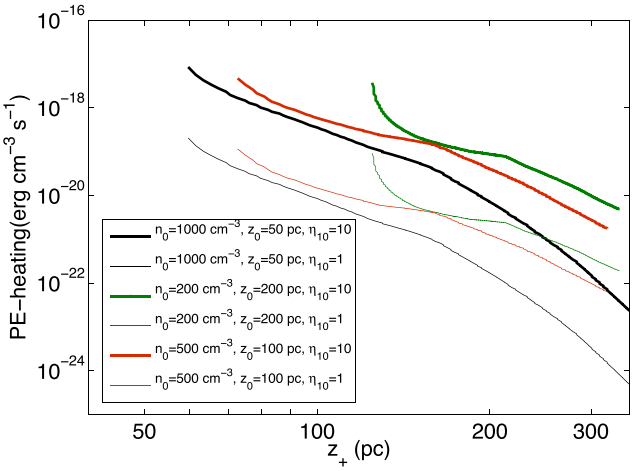

Figure D1. The time evolution of the heating rate in superbubble shell at the time when its uppermost position is z_+, for three different n_0, z_0 cases ($n_0 = 1000$ cm^{-3}, $z_0 = 50$ pc; $n_0 = 200$ cm^{-3}, $z_0 = 200$ pc, and $n_0 = 500$ cm^{-3}, $z_0 = 100$ pc), for two η_{10} cases and for $N_{\rm OB} = 10^5$. The thick and thin solid lines correspond to $\eta_{10} = 10$ and 1, respectively. The black, green, and the red lines represent $n_0 = 1000$ cm^{-3}, $z_0 = 50$ pc; $n_0 = 200$ cm^{-3}, $z_0 = 200$ pc, and $n_0 = 500$ cm^{-3}, $z_0 = 100$ pc cases, respectively.

heating (PE-heating) and cooling balance. Thus, one needs to solve the equations of ionization and thermal equilibrium simultaneously to obtain $n_{\rm e}$, and $T_{\rm shell}$, and to understand their effect on PE-heating rate. The electron density ($n_{\rm e}$) has a strong dependence on the shell density, thus $n_{\rm e}$ decreases as the shell density decreases. Therefore, the PE-heating rate also drops initially. In all these three n_0-z_0 combinations the shell radius reaches at $\sim$200 pc in 2−3 Myr, when the FUV photon luminosity starts dropping drastically, and thus we notice kinks in the curves of PE-heating rates at $\sim$200 pc, and PE-heating rate drops after 200 pc due to the drop in $S_{\rm FUV}$.

We use the same cooling function as in our simulation for the dynamics of the superbubbles, the details of which are described in Section A.

APPENDIX E: DENSITY AND TEMPERATURE IN THE DENSE SHELL

The heating and cooling time-scales in the shell are shorter than the dynamical time-scale (z_+/t) at all times. Thus, one can assume thermal equilibrium to calculate the shell temperature.

First we show the ionization fraction, total gas density and electron density in the shell in Fig. E1. The nature of the curve for $n_{\rm e}$ mimics that of the curve for the total shell density, $n_{\rm sh}$, albeit with small differences which show clearly in the plot for $x_{\rm e}$, the ionization fraction. Here again there are kinks in the curves at $\sim$200 pc, and they arise because of the change in the FUV luminosity as mentioned earlier.

Next, we show the equilibrium shell temperature as a function of the position of the shell in Fig. E2, for three different combinations of n_0, z_0 and for $N_{\rm OB} = 10^5$. In the case of larger scaleheight (200 pc),

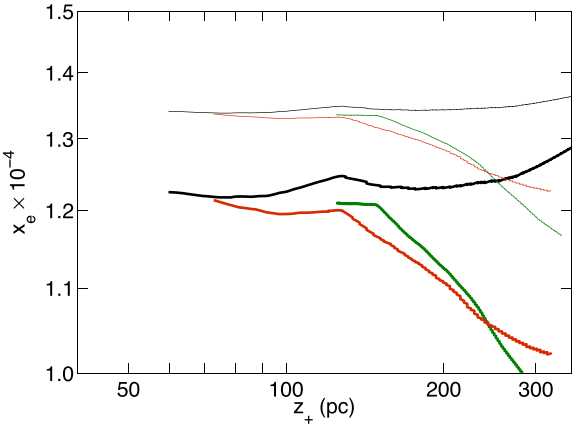

Figure E1. The evolution of the ionization fraction as a function of the vertical height of the superbubble. All the line-styles and line-colours representing different n_0, z_0, and η_{10} are mentioned in the caption of Fig. D1.

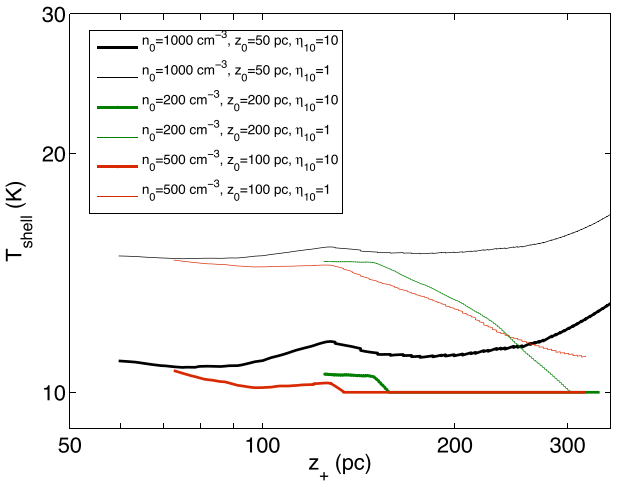

Figure E2. The equilibrium temperature of the shell is plotted as a function of the shell-radius for three different n_0, z_0 cases for $N_{\rm OB} = 10^5$, and for $\eta_{10} = 1$ and 10.

the shell temperature initially is $\sim$10−20 K, and it falls to $\sim$10 K at larger radii. This is owing to the high density in the shell, and consequently, greater cooling. In the case of smaller scaleheight, the low density at large heights, the ionization fraction increases and so does PE heating, and thus the shell temperature increases with radius. Again, kinks arise due to the nature of FUV luminosity evolution.

This paper has been typeset from a TEX/LATEX file prepared by the author.